Materials Today Communications 38 (2024) 108431

Contents lists available at ScienceDirect

Materials Today Communications

journal homepage: www.elsevier.com/locate/mtcomm

Phase-field simulation of α-α′ phase separation in nuclear Fe-Cr-Al-based alloys induced by chemical composition and irradiation

Ben Niu [a], Zhen Li [b,*], Qing Wang [a,*], Zhenhua Wang [a], Sen Ge [a], Chuang Dong [a], Ruiqian Zhang [c,*], Donghui Wen [d], Huiqun Liu [e], Peter K. Liaw [f]

[a] School of Materials Science and Engineering, Engineering Research Center of High Entropy Alloy Materials (Liaoning Province), Dalian University of Technology, Dalian, Liaoning 116024, China
[b] School of Mechanical Engineering, Dalian University of Technology, Dalian, Liaoning 116024, China
[c] Science and Technology on Reactor Fuel and Materials Laboratory, Nuclear Power Institute of China, Chengdu, Sichuan 610213, China
[d] School of Materials Science and Engineering, Dongguan University of Technology, Dongguan 523808, China
[e] School of Materials Science and Engineering, Central South University, Changsha, Hunan 410083, China
[f] Department of Materials Science and Engineering, The University of Tennessee, Knoxville, TN 37996, USA

ARTICLE INFO

Keywords:
Nuclear Fe-Cr-Al-based alloys
Phase-field simulation
Phase separation
Microstructural evolution
Irradiation

ABSTRACT

The present work applied the phase-field (PF) method to comprehensively investigate the effects of chemical composition and irradiation on the α-α′ phase separation in nuclear Fe-Cr-Al-based alloys since it is difficult to be clarified by experiments alone. Three series of alloys were designed by changing the amount of Cr, Al, and Mo in sequence, being Fe-xCr-9.375Al, Fe-15.625Cr-xAl, and Fe-(15.625-x)Cr-9.375Al-xMo (at%). The PF simulation was based on the Cahn-Hilliard equation, in which a radiation-enhanced model was embedded to consider the atomic mobility of alloying elements under irradiation. The results indicated that the Cr element can accelerate the α-α′ phase separation, as demonstrated by the increase in volume fraction (5.1% in 15Cr and 12.6% in 40Cr) and the reduction in incubation time of α′ nanoprecipitates (5000 h in 15Cr and 200 h in 28Cr) during aging at 573 K, while Al and Mo inhibit the phase separation effectively due to an obvious extension of the incubation time (5×10^4 h in 1.7Mo). Coupled with the irradiation, the phase separation will be speeded up significantly with a severe shrinkage of the incubation time to 2 ~ 388 h (0.14 ~ 0.5 dpa) in 15Cr. The mechanisms on the α-α′ phase separation were then discussed from both thermodynamic and kinetic viewpoints, in which the incubation time is closely related to the driving force of α→(α+α′) and the atomic mobility of Cr. The present PF simulation can provide an important method to predict the α-α′ phase separation in novel nuclear Fe-Cr-Al-based alloys.

1. Introduction

The Fe-Cr-Al-based alloys have attracted more attention for serving as fuel-cladding materials due to their prominent mechanical properties and resistances to steam oxidation and corrosion, as well as good neutron-irradiation resistance [1–3]. However, the severe embrittlement problem always occurs in this kind of alloys at the temperature of 573 ~ 773 K, i.e., the classical 748 K-embrittlement [4,5], which has been identified to be induced by the phase separation of the body-centered-cubic (BCC) ferritic solid-solution matrix into the Fe-rich ferritic phase (BCC α-Fe) and the Cr-rich phase (BCC α′-Cr) in the miscibility gap [6,7]. The α-α′ phase separation could not only enhance the microhardness drastically and then lead to an alloy brittleness, but also accelerate the corrosion behavior due to the segregation of Cr element. It was emphasized that both the species and added amounts of alloying elements could affect the α-α′ phase separation, as well as the related embrittlement of Fe-Cr-Al-based alloys [8–11]. In particular, the increase of Cr content can accelerate the α-α′ phase separation. It is difficult to induce the phase separation in low-Cr Fe-10Cr-(4−8)Al (wt%) alloys even after aging at 773 K for 10,000 h [11], while a large amount of α′ nanoparticles could precipitate in high-Cr Fe-15Cr-4.5Al (wt%) alloy after aging at 748 K for 10,000 h with a volume fraction of f ~ 3.2% and a particle size of r ~ 4.0 nm [8]. Based on which, the further increase of Al could inhibit the α-α′ phase separation, as evidenced by the fact that when the Al content in the Fe-15Cr-4.5Al alloy was increased to 6 wt%, the α′ phase disappeared and no obvious enrichment of the Cr

* Corresponding authors.
E-mail addresses: lizhen@dlut.eud.cn (Z. Li), wangq@dlut.edu.cn (Q. Wang), zhang_ruiqian@126.com (R. Zhang).

https://doi.org/10.1016/j.mtcomm.2024.108431
Received 8 December 2023; Received in revised form 4 February 2024; Accepted 18 February 2024
Available online 20 February 2024

Table 1
Chemical compositions of the designed nuclear Fe-Cr-Al-Mo alloys used for phase-field simulations.

Alloy series	No.	Cluster formula	at%
Cr-series	15Cr	Fe_{12}-$Cr_{2.5}$-$Al_{1.5}$	$Fe_{75}Cr_{15.625}Al_{9.375}$
Fe-xCr-9.375Al	22Cr	Fe_{11}-$Cr_{3.5}$-$Al_{1.5}$	$Fe_{68.75}Cr_{21.875}Al_{9.375}$
	28Cr	Fe_{10}-$Cr_{4.5}$-$Al_{1.5}$	$Fe_{62.5}Cr_{28.125}Al_{9.375}$
	40Cr	Fe_{8}-$Cr_{6.5}$-$Al_{1.5}$	$Fe_{50}Cr_{40.625}Al_{9.375}$
Al-series	6Al	$Fe_{12.5}$-$Cr_{2.5}$-Al_{1}	$Fe_{78.125}Cr_{15.625}Al_{6.25}$
Fe-15.625Cr-xAl	8Al	$Fe_{12.2}$-$Cr_{2.5}$-$Al_{1.3}$	$Fe_{76.25}Cr_{15.625}Al_{8.125}$
	12Al	$Fe_{11.5}$-$Cr_{2.5}$-Al_{2}	$Fe_{71.875}Cr_{15.625}Al_{12.5}$
Mo-series	0.3Mo	Fe_{12}-$[Cr_{50}Mo_{1}]_{2.5}$-$Al_{1.5}$	$Fe_{75}Cr_{15.315}Al_{9.375}Mo_{0.31}$
Fe-(15.625-x)Cr-9.375Al-xMo	1.0Mo	Fe_{12}-$[Cr_{14}Mo_{1}]_{2.5}$-$Al_{1.5}$	$Fe_{75}Cr_{14.583}Al_{9.375}Mo_{1.042}$
	1.7Mo	Fe_{12}-$[Cr_{8}Mo_{1}]_{2.5}$-$Al_{1.5}$	$Fe_{75}Cr_{13.889}Al_{9.375}Mo_{1.736}$

Table 2
Related parameters for the calculation of irradiation-enhanced diffusion coefficients [47–50].

Vacancy concentration	X_V^e	1.0×10^{-11} m^{-3}
Displacement-per-atom cross-section	σ_{dpa}	1.5×10^{-25} m^2 [47]
Vacancy migration energy	E_m	1.1 eV [48]
Dislocation sink strength	S_d	1×10^{13} m^{-2} [48]
Boltzmann constant	k	1.38×10^{-23} $J{\cdot}K^{-1}$
Saturated sink strength of vacancy clusters	S_c	3×10^{15} m^{-2} [48]
Empirical scaling exponent	p	0.2 [49]
Cascade efficiency	ξ	0.33 (neutron or ion irradiation) [50]

element was found in the Fe-15Cr-6Al alloy after aging 748 K for 10, 000 h [12]. In addition, a minor amount of Mo and Nb elements were often added into the Fe-Cr-Al alloys to precipitate the Fe_2(Mo,Nb) Laves phase for strengthening the matrix, which does not affect the α-α′ phase separation due to their limited solubility in the BCC matrix [13]. On the other side, it was also found that the irradiation can accelerate significantly the phase separation in Fe-Cr-Al alloys [9,14,15], as exemplified by the fact that the α′ precipitates ($r \sim 1.5$ nm and $f \sim 5.8\%$) were obviously observed in the Fe-14.7Cr-3.92Al (wt%) alloy after being neutron-irradiated to 7.0 dpa at 593 K (for 2456 h) [9]. Even for the low-Cr Fe-9.85Cr-4.75Al (wt%) alloy, the volume fraction of α′ phase after the same irradiation could reach to $f \sim 1.5\%$, where the phase separation did not occur after thermal-aging alone [9].

Up to now, the research on α-α′ phase separation (or α′ phase precipitation) in Fe-Cr-Al-based alloys was mainly dependent on advanced characterization techniques, such as transmission electron microscopy (TEM) [8,16], atom probe tomography (APT) [10,14], and small-angle neutron scattering (SANS) [9], etc. Although these experimental techniques play an important role in observing this phenomenon, it is still difficult to understand the intrinsic mechanism of phase separation and the microstructural evolution. Recently, the phase-field (PF) method has been become a powerful computational approach to deal with many types of microstructural variations, such as simulating the morphological evolution of the second-phase precipitation [17–19]. Meanwhile, it can contribute to the underlying mechanisms during the solidification and the solid-solid phase transformations. A classical instance is that the microstructural evolution of coherent γ and γ′ phases in Ni-base superalloys was well simulated by the PF method, including the coarsening of γ′ particles during long-term aging and the particle rafting under an applied stress field [20,21]. Also, it has been successfully applied to elucidate the variation of particle morphologies with chemical compositions in Al-Fe-Co-Ni-Cr high-entropy alloys containing BCC/B2 coherent microstructures [17]. These simulations can provide a significant support for profoundly understanding of experimental results. For the Fe-Cr-Al alloys, the existing studies mainly focused on the PF simulation of phase separation in high-Cr (> 20 at%) alloys under heat-treated conditions at different temperatures [22–24]. For example, the PF simulation of Fe-38Cr-10Al (at%) alloy revealed the effect of temperature (720 ~ 760 K) on the α-α′ phase separation [24]. However, few research activities reported on the phase evolution in nuclear Fe-Cr-Al alloys with a relatively-low Cr content (< 20 at%) under the operating conditions (both temperature and irradiation), which is necessary to understand the intrinsic mechanism of phase separation using the PF method.

In fact, it is crucial to tailor the content of each alloying element (Cr, Al, Mo, Nb, etc.) in nuclear Fe-Cr-Al-based alloys for the achievement of excellent comprehensive properties at high temperatures. And it is more necessary to investigate the possibility of α-α′ phase separation in these alloys since it is sensitive to the contents of Cr and Al. However, the effects of a small amount of element addition and irradiation conditions on the phase separation have not been clarified due to the difficulty of the experimental verification, which is important for the development of novel nuclear Fe-Cr-Al-based alloys. The PF method can well simulate the α-α′ phase separation, which will be helpful to understand the dynamic-evolution process, especially under the condition of multi-field coupling (temperature and irradiation). Therefore, the PF method with a radiation-enhanced diffusion model will be applied to investigate the microstructural evolution induced by the α-α′ phase separation in nuclear Fe-Cr-Al-based alloys. The effects of the amounts of Cr, Al, and Mo elements, as well as the irradiation dose and dose rate on the precipitation and coarsening of α′ nanoparticles will be emphasized and discussed from the viewpoints of thermodynamics and kinetics. Finally, the PF simulations will be compared with the existing experimental results to uncover the key factors to affect the α-α′ phase separation.

2. Composition design of Fe-Cr-Al-based alloys

Experimentally, the best composition range of ternary nuclear Fe-Cr-Al alloys possessing the optimum mechanical property and corrosion/oxidation resistances was determined as Fe-(13−15)Cr-(4−5)Al (wt%, = Fe-(13.1–15.3)Cr-(7.8–9.7)Al at%), based on which the addition of Mo can further improve the comprehensive properties of Fe-13Cr-4.5Al-2Mo alloy (wt%, = Fe-13.3Cr-8.8Al-1.1Mo at%) [1]. It is known that the chemical short range orders (CSROs) induced by the local distribution of solute atoms are the typical characteristics of solid-solution alloys, which is different from the average structure and could enhance alloy properties [25]. In light of the CSROs, we proposed a cluster-plus-glue-atom model to describe the local distributions of solute atoms in multi-component alloy systems, which can give a simple cluster formula of [cluster](glue atoms)$_m$ (one cluster matching with m glue atoms) to design alloy compositions [26,27]. Generally, the cluster is the nearest-neighbor polyhedron centered by the solute atom having a stronger interaction with the base solvent atoms, and the other solute atoms having relatively-weaker interaction with the base atoms serve as the glue atoms to link the isolated clusters for the balance of the alloy density [26,27]. Specifically, the current Fe-Cr-Al ternary alloys could be rewritten with the cluster formula of [Al-($Fe_{12}Cr_2$)]($Al_{0.5}Cr_{0.5}$) (= $Fe_{12}Al_{1.5}Cr_{2.5}$ = $Fe_{75}Al_{9.375}Cr_{15.625}$ at%), in which the cluster is the rhombic dodecahedron with the coordination number of CN14 in the BCC structure, centered by Al and surrounded by twelve Fe atoms and two Cr atoms since the interactions between Al-Fe and Al-Cr are comparable. Both Al and Cr with an equi-molar ratio serve as one glue atom, which is inspired by the high-entropy alloying principle that is the most fashionable in developing high-performance advanced alloy materials [28]. Actually, our previous works have verified that the Fe-13.5Cr-4.73Al-2.07Mo-(0.34–0.5)Nb-(0.65–0.98)Ta-(0–0.33)Zr (wt%) alloys designed via the cluster formula show high microstructural stability at high temperatures [29], and the yield strength can remain above 80 MPa even at 1073 K, which is obviously higher than those (50 ~ 70 MPa) of existing Fe-Cr-Al-based alloys [1,13]. Therefore, based on the basic cluster formula of $Fe_{12}Al_{1.5}Cr_{2.5}$ (designated as 15Cr due to the

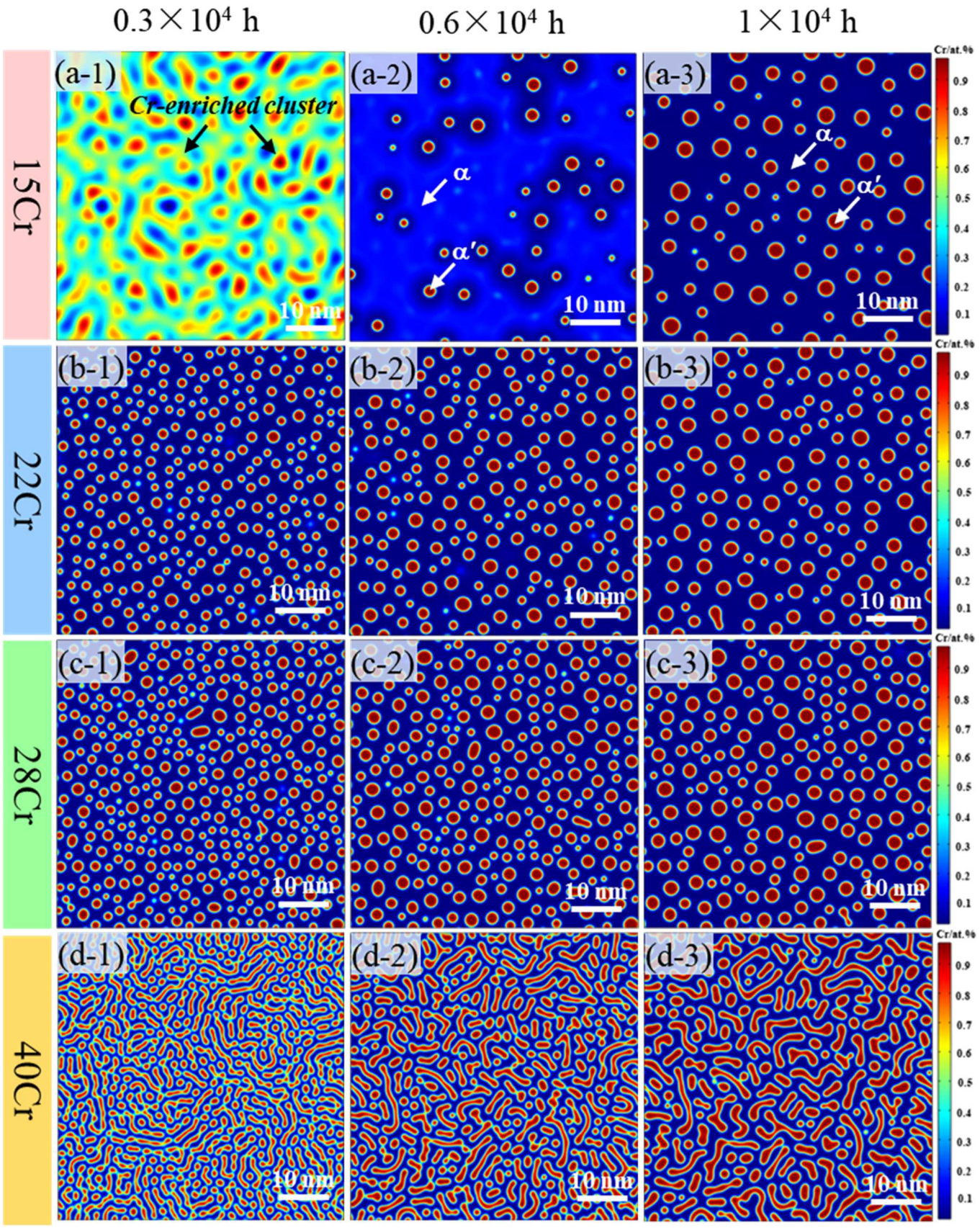

Fig. 1. Evolution of α′-phase precipitation in Fe-xCr-9.375Al (at%) alloys (Cr-series) with the aging time t at 573 K. (a): x = 15.625 (15Cr), (b): x = 21.875 (22Cr), (c): x = 28.125 (28Cr), (d): x = 40.625 (40Cr), and (1): $t = 0.3\times10^4$ h, (2): $t = 0.6\times10^4$ h, (3): $t = 1\times10^4$ h.

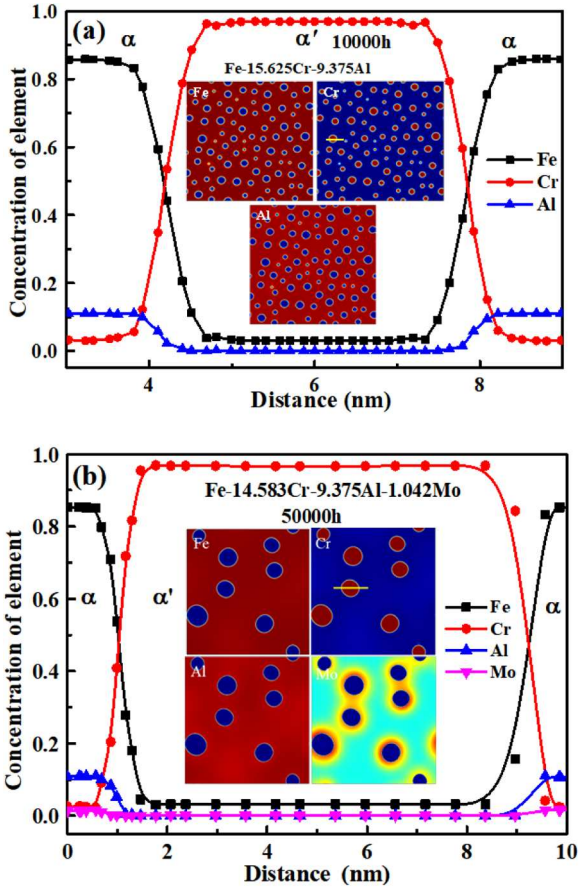

Fig. 2. Concentration distributions of elements (Fe, Cr, Al, Mo) in the α′ phase for typical Fe-15.625Cr-9.375Al (a) and Fe-14.583Cr-9.375Al-1.042Mo (b) alloys.

content of Cr being 15.625 at%), we increased the Cr content by substituting the Cr ($Cr_{3.5}$, $Cr_{4.5}$, and $Cr_{6.5}$ in the cluster formula) for the base Fe and fixing the Al to form the Cr-series of ternary alloys, Fe-xCr-9.375Al (at%), being designated as 22Cr, 28Cr, and 40Cr, respectively. In order to study the effect of Al element on the α-α′ phase separation, we also changed the Al content (Al_1, $Al_{1.3}$, and Al_2 in the cluster formula) based on the $Fe_{12}Al_{1.5}Cr_{2.5}$ to form the Al-series of alloys, Fe-15.625Cr-xAl (at%), being designated as 6Al, 8Al, and 12Al, respectively. Moreover, a small amount of Mo element was added to replace the Cr in the basic $Fe_{12}Al_{1.5}Cr_{2.5}$ formula to form the Mo-series of quaternary alloys, Fe-(15.625-x)Cr-9.375Al-xMo (at%), being designated as 0.3Mo, 1.0Mo, and 1.7Mo, in which the ratio of Mo to Cr was determined by the nearest-neighbor distribution of solute atoms in the BCC solid-solution structure [26]. Table 1 gives the chemical compositions (at%) of these three designed alloy series, which will be used for the phase-field simulation.

3. Phase-field model

3.1. Microscopic phase-field model

Generally, the α-α′ phase separation in the Fe-Cr-Al-based alloys were simulated by the evolution of the concentration field, $c(\boldsymbol{r}, t)$, which is controlled by the Cahn-Hilliard nonlinear diffusion equation (Eq. (1)) [30]:

$$\frac{\partial_{C_{Cr}}(\boldsymbol{r},t)}{\partial_t} = V_m\nabla(M_{CrCr}\nabla\frac{\delta F}{\delta c_{Cr}} + M_{CrAl}\nabla\frac{\delta F}{\delta c_{Al}} + M_{CrMo}\nabla\frac{\delta F}{\delta c_{Mo}})$$

$$\frac{\partial_{C_{Al}}(\boldsymbol{r},t)}{\partial_t} = V_m\nabla(M_{AlCr}\nabla\frac{\delta F}{\delta c_{Cr}} + M_{AlAl}\nabla\frac{\delta F}{\delta c_{Al}} + M_{AlMo}\nabla\frac{\delta F}{\delta c_{Mo}}) \quad (1)$$

$$\frac{\partial_{C_{Mo}}(\boldsymbol{r},t)}{\partial_t} = V_m\nabla(M_{MoCr}\nabla\frac{\delta F}{\delta c_{Cr}} + M_{MoAl}\nabla\frac{\delta F}{\delta c_{Al}} + M_{MoMo}\nabla\frac{\delta F}{\delta c_{Mo}})$$

where $c_i(\boldsymbol{r}, t)$ denotes the nominal composition of the i element (i = Fe, Cr, Al, Mo), r and t are the spatial coordinates and time, V_m is the molar volume, M is the chemical mobility, and the total free energy, F, can be expressed with Eq. (2) [31,32]:

$$F = \int_v \left\{\frac{1}{V_m}[G + \kappa_{Fe}(\nabla c_{Fe})^2 + \kappa_{Cr}(\nabla c_{Cr})^2 + \kappa_{Al}(\nabla c_{Al})^2 + \kappa_{Mo}(\nabla c_{Mo})^2]\right\}\mathrm{d}V \quad (2)$$

where G is the molar Gibbs energy, κ_i is the gradient-energy coefficient of the i element. To simplify the calculation, the κ_i values are always assumed as $\kappa_{Fe} = \kappa_{Cr} = \kappa_{Al} = \kappa_{Mo} = a_0^2 * L_{FeCr}/6$, in which the a_0 and L_{FeCr} are the interatomic distance and the interaction parameter between Fe and Cr, respectively. And the expression for the G is expressed with Eq. (3) [33]:

$$\begin{aligned} G =& c_{Fe}G_{Fe} + c_{Al}G_{Al} + c_{Cr}G_{Cr} + c_{Mo}G_{Mo} + L_{FeCr}c_{Fe}c_{Cr} + L_{CrAl}c_{Cr}c_{Al} \\ &+ L_{FeAl}c_{Fe}c_{Al} + L_{FeMo}c_{Fe}c_{Mo} + L_{CrMo}c_{Cr}c_{Mo} + L_{AlMo}c_{Al}c_{Mo} \\ &+ RT\ln(c_{Fe}\ln c_{Fe} + c_{Cr}\ln c_{Cr} + c_{Al}\ln c_{Al} + c_{Mo}\ln c_{Mo}) \end{aligned} \quad (3)$$

where G_i is the molar Gibbs energy of the i element of pure state (reference state) [34], R is the gas constant, T is the absolute temperature, and L_{ij} is the interaction parameter between different elements [35–37]. All of these parameters are all interpreted in the Supplementary Materials. In addition, the M_{ij} in Eq. (1) is determined by the atomic mobility shown in Eq. (4) [38,39]:

$$\begin{aligned} M_{Cr,Cr} &= c_{Cr}[(1-c_{Cr})^2 M_{Cr} + c_{Cr}c_{Al}M_{Al} + c_{Cr}c_{Fe}M_{Fe} + c_{Cr}c_{Mo}M_{Mo}] \\ M_{Al,Al} &= c_{Al}[(1-c_{Al})^2 M_{Al} + c_{Al}c_{Cr}M_{Cr} + c_{Al}c_{Fe}M_{Fe} + c_{Al}c_{Mo}M_{Mo}] \\ M_{Mo,Mo} &= c_{Mo}[(1-c_{Mo})^2 M_{Mo} + c_{Mo}c_{Cr}M_{Cr} + c_{Mo}c_{Fe}M_{Fe} + c_{Al}c_{Mo}M_{Mo}] \\ M_{Cr,Al} &= c_{Cr}c_{Al}[c_{Fe}M_{Fe} - (1-c_{Al})M_{Al} - (1-c_{Cr})M_{Cr} + c_{Mo}M_{Mo}] \\ M_{Cr,Mo} &= c_{Cr}c_{Mo}[c_{Fe}M_{Fe} + c_{Al}M_{Al} - (1-c_{Cr})M_{Cr} - (1-c_{Mo})M_{Mo}] \\ M_{Al,Mo} &= c_{Al}c_{Mo}[c_{Fe}M_{Fe} + c_{Cr}M_{Cr} - (1-c_{Al})M_{Al} - (1-c_{Mo})M_{Mo}] \end{aligned} \quad (4)$$

where M_i is the atomic mobility of the i element and determined with Eq. (5) [40]:

$$M_i = \exp(\frac{RT\ln M_i^0 - Q_i}{RT})\frac{1}{RT} \quad (5)$$

where M_i^0 and Q_i are the frequency and activation energy of the i element. Supposing that $\varnothing_\alpha = RT\ln M_i^0 - Q_i$ (α = Fe, Cr, Al, Mo), the specific formula is described with Eq. (6) [41]:

$$\begin{aligned} \varnothing_\alpha =& \sum_i c_i\varnothing_\alpha^i + \sum_i\sum_{j>i} c_ic_j\left[\sum_{r=0}^{m} {}^r\varnothing_\alpha^{i,j}(c_i - c_j)^r\right] \\ &+ \sum_i\sum_{j>i}\sum_{k>j} c_ic_jc_k\left[v_{ijk}^s \; {}^s\varnothing_\alpha^{i,j,k}\right] \end{aligned} \quad (6)$$

where $\varnothing_\alpha^i$ is the value of the α element in a pure i element, ${}^r\varnothing_\alpha^{i,j}$ and ${}^s\varnothing_\alpha^{i,j,k}$ are the binary and ternary interaction parameters. For simplicity, the ternary interaction parameters among three elements in Eq. (6) was generally neglected, where the detailed calculations for the related parameters were presented in the Supplementary Materials [42–45].

The above parameters should be non-dimensionalized for the simu-

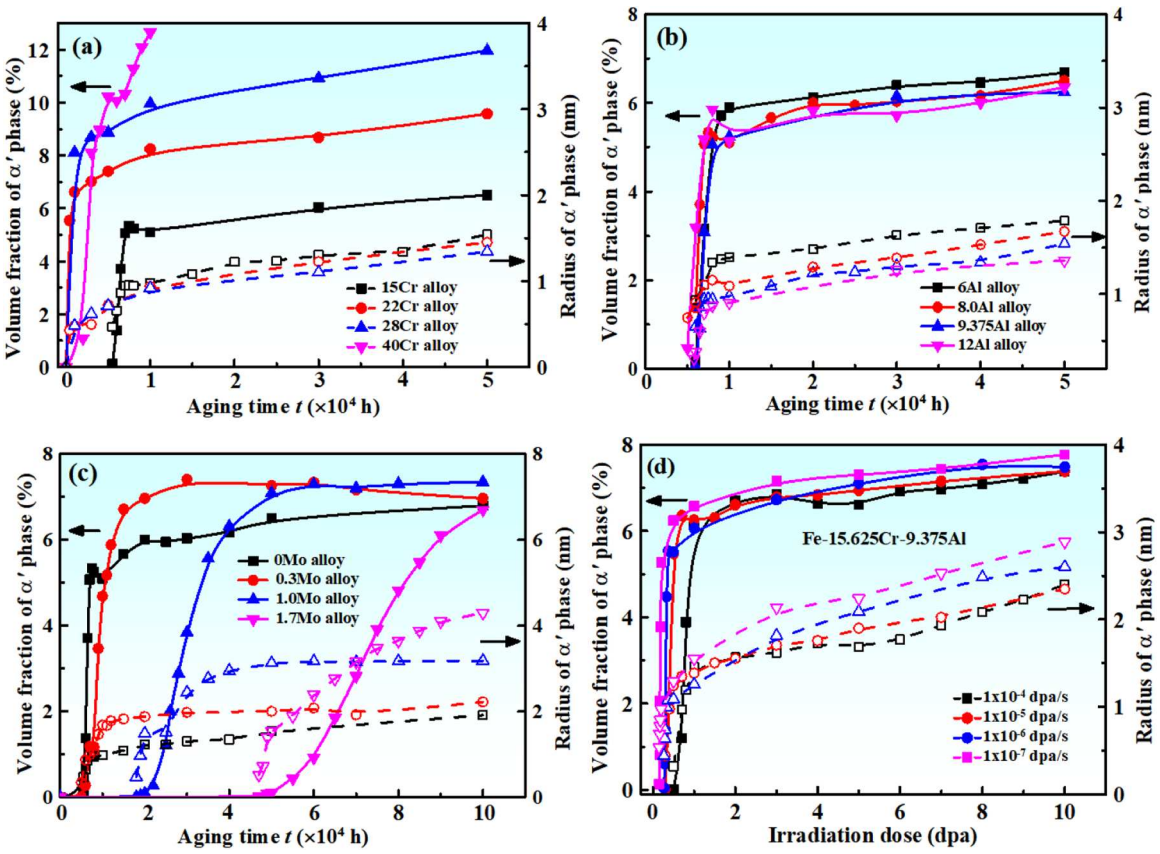

Fig. 3. Variations of the average particle size and volume fraction of α′ nanoprecipitates in different alloy series, Fe-xCr-Al (Cr-series, a), Fe-Cr-xAl (Al-series, b), and Fe-Cr-Al-Mo (Mo-series, c) with the aging time at 573 K, and with the irradiation dose in Fe-15.625Cr-9.375Al alloy (d) at different dose rates.

lation, being:

$$r^* = r/l$$

$$t^* = tD/l^2$$

$$M_{ij}^* = RT_0M_{ij}/D \tag{7}$$

$$G^* = G/RT_0$$

$$\kappa^* = \kappa/RT_0l^2$$

$$l = a_0 = a_{Fe}c_{Fe} + a_{Cr}c_{Cr} + a_{Al}c_{Al} + a_{Mo}c_{Mo}$$

where the lattice parameters are $a_{Fe} = 2.866\times10^{-10}$ m, $a_{Cr} = 2.882\times10^{-10}$ m, $a_{Al} = 4.049\times10^{-10}$ m, and $a_{Mo} = 3.146\times10^{-10}$ m [46], respectively. $D = 2.4\times10^{-25}$ m^2/s is adopted as the normalization factor, and $T_0 = 875$ K is the critical temperature for the α-α′ phase separation in the Fe-Cr-Al-based alloys. To induce this phase separation, a random thermal fluctuation with a magnitude of [−0.002, 0.002] was introduced into the initial composition, and the time step is $\Delta t^* = 1$.

3.2. Radiation-enhanced diffusion

In order to investigate the α-α′ phase separation in the Fe-Cr-Al-based alloys under an irradiation environment, we coupled the radiation-enhanced diffusion (RED) model developed by Odette into the PF method [47]. The ballistic effect is not considered because the irradiation acceleration effect is much greater than the ballistic effect in low Cr alloys. In the RED model, the expression of the atomic mobility was modified by considering the vacancy concentration under irradiation and the effect of vacancy on the atomic-diffusion coefficient, which is expressed with Eq. (8) [48]:

$$M = X_V^r\frac{M^{th}}{X_V^e} + M^{th} \tag{8}$$

where M^{th} is the atomic mobility without irradiation, X_V^r is the non-equilibrium vacancy concentration under irradiation condition, and X_V^e is the vacancy concentration in a thermodynamic equilibrium state. Among them, the expression of X_V^r can be written with Eq. (9) [47]:

$$X_V^r = \frac{g_s\xi\sigma_{dpa}\varphi}{D_VS_t} \tag{9}$$

where g_s is the vacancy-survival fraction, σ_{dpa} is the dpa cross-section, φ is the irradiation flux, ξ is the cascade efficiency, S_t is the total sink strength, including the contributions from both the dislocations (S_d) and vacancy clusters (S_c). The former can be characterized by the dislocation density and the latter can obtained by the saturated sink strength of vacancy clusters. D_V is the vacancy-diffusion efficient and expressed with Eq. (10) [48]:

$$D_V = 10^{-4}\exp[-E_m/(kT)] \tag{10}$$

where E_m is the vacancy-migration energy. And we chose a much simpler expedient to calculate the g_s as a function of the irradiation flux φ, which has been applied widely, being described with Eq. (11) [49]:

$$g_s(\varphi) = g_s(\varphi_r)(\varphi_r/\varphi)^p \tag{11}$$

where $\varphi_r = 3\times10^{15}$ m^{-2}/s is determined as the low reference flux, and $p = 0.2$ is an empirical scaling exponent. It is noted that the $g_s(\varphi_r)$ is always close to 1 at a low flux (negligible recombination) [49]. All these parameter values involved in the RED model are listed in Table 2 [47–50].

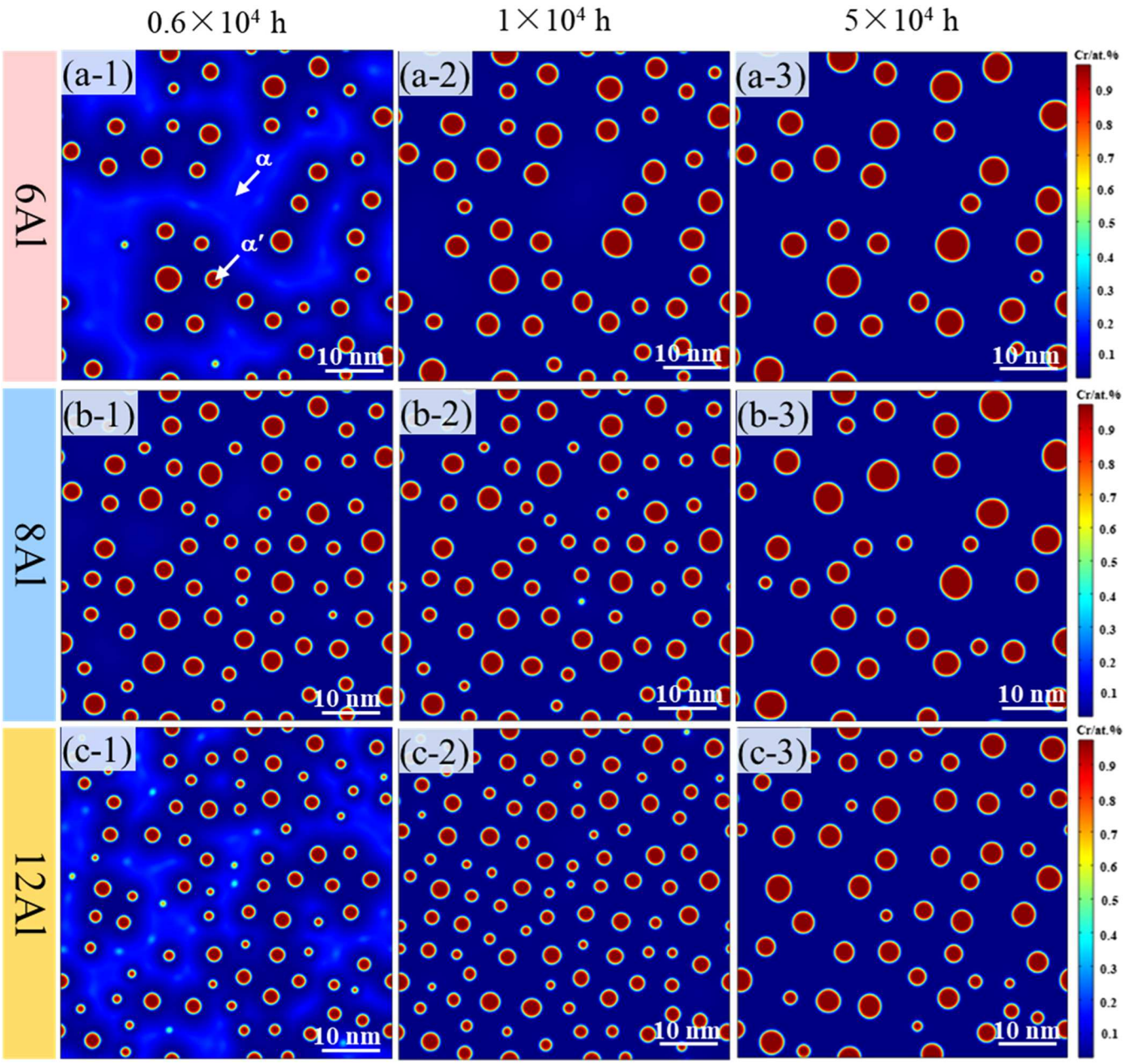

Fig. 4. Evolution of α′ nanoprecipitates in Fe-15.625Cr-xAl (at%) alloys (Al-series) with aging time at 573 K. (a): x = 6.25 (6Al), (b): x = 8.125 (8Al), (c): x = 12.5 (12Al), and (1): $t = 0.6\times10^4$ h, (2): $t = 1\times10^4$ h, (3): $t = 5\times10^4$ h.

3.3. Description of phase-field simulations

The microscopic PF model was employed to simulate the α′ precipitation (α-α′ phase separation) of Fe-Cr-Al and Fe-Cr-Al-Mo alloys with different Cr, Al, and Mo contents at 573 K. The simulation cells are 200 × 200 and 250 × 250 for ternary alloys (Cr series and Al series) and quaternary alloys (Mo series), respectively, in which the length of one cell represents 0.3 nm. And periodic boundary conditions were employed along each direction. Moreover, the PF model under irradiation conditions by coupling both the Cahn-Hilliard and RED equations was employed to simulate the α′ precipitation in the current alloys at 573 K with the irradiation dose up to 10 dpa and the dose rate of $1\times10^{-7} \sim 1\times10^{-4}$ dpa/s. In order to simulate the α-α′ phase separation, we will solve the Cahn-Hilliard equation with the finite element method, which is executed by the partial differential equation (PDE) module in a COMSOL Multiphysics software [51]. The time t in the result is obtained by bringing the simulation output time step t^* into Eq. (7), i.e., $t = t^* l^2/D$. The statistical analysis of the particle morphology of precipitates in different states were measured from the simulated images using the Image-Pro Plus 6.0 software, in which the volume fraction of particles was estimated by the projected areal fraction, A_f, i.e., $f = 2A_f/3$, and the average particle size was estimated by $r = \sqrt{\frac{A_f}{\pi n}}$ (n is the number of precipitated particles).

4. Results

4.1. Precipitation of the α′ phase in designed alloys at 573 K without irradiation

4.1.1. α′ precipitation in Cr-series of alloys

Fig. 1 presents the evolution of α′ precipitates in the designed Cr-series of alloys (15Cr, 22Cr, 28Cr, and 40Cr) with the aging time (0.3

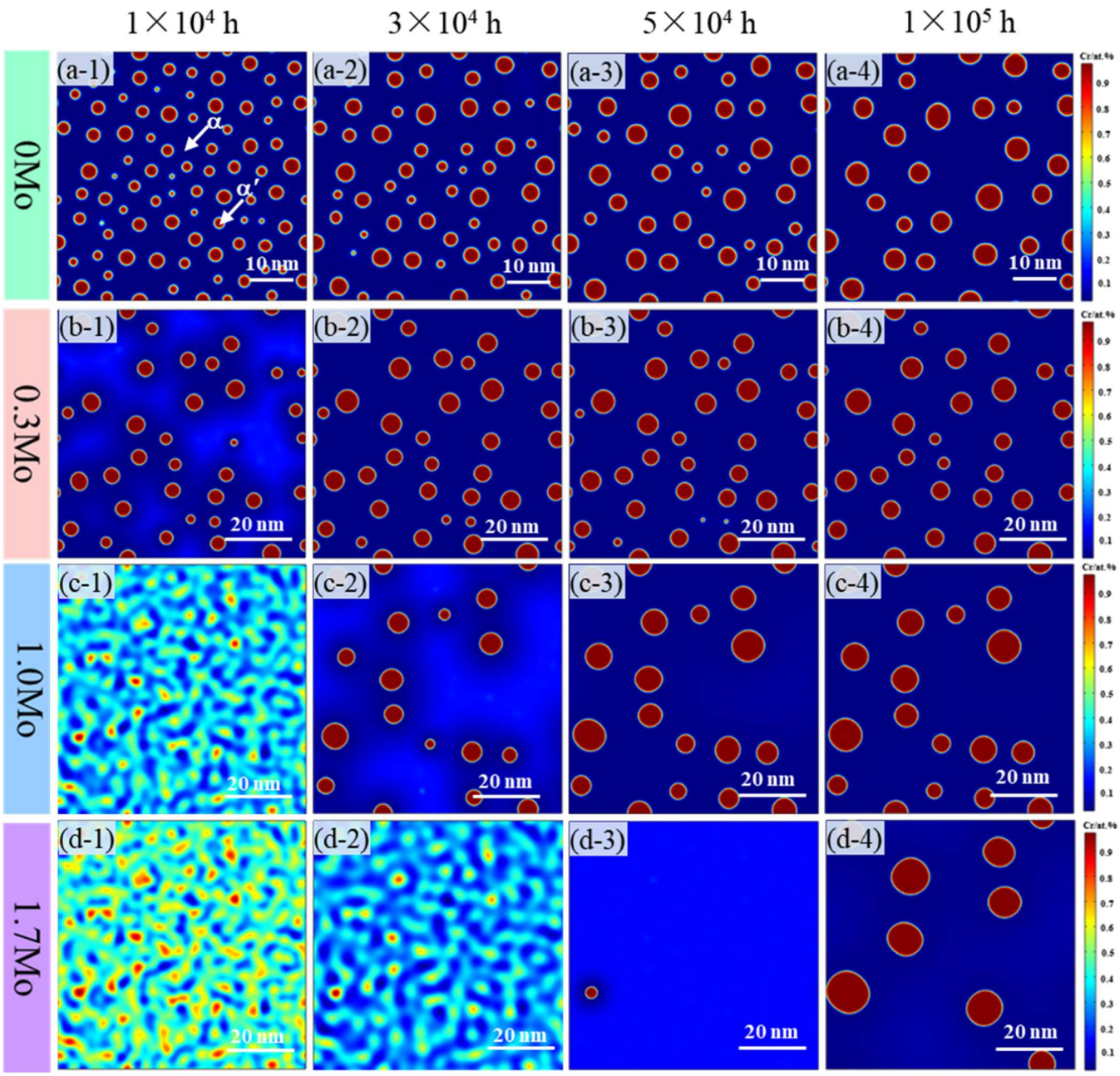

Fig. 5. Evolution of α′ nanoprecipitates in Fe-(15.625-x)Cr-9.375Al-xMo (at%) alloys (Mo-series) with aging time at 573 K. (a): x = 0.31 (0.3Mo), (b): x = 1.042 (1.0Mo), (c): x = 1.736 (1.7Mo), and (1): $t = 1\times10^4$ h, (2): $t = 3\times10^4$ h, (3): $t = 5\times10^4$ h, (4): $t = 1\times10^5$ h.

$\sim 1\times10^4$ h) at 573 K. The red and blue colors represent the Cr-rich α′ phase and Fe/Al-rich BCC-α ferritic matrix, respectively, in which the two-dimensional domain boundaries are periodic in every direction. It is emphasized that the Cr concentration in the α′ phase is higher than 90 at %, while the Al element is obviously segregated into the BCC-α matrix, as seen in Fig. 2(a). When the Cr content is lower, it is difficult to precipitate the α′ nanoparticles in the 15Cr alloy ($Fe_{75}Cr_{15.625}Al_{9.375}$ at%) after 0.3×10^4 h-aging, but the Cr-enriched clusters appear, as presented by the black arrows in Fig. 1(a-1). With increasing the aging time to 0.6×10^4 h, the spherical α′ nanoparticles precipitate from the α matrix with an average size of $r = 0.7$ nm and a lower volume fraction of $f = 1.4\%$ (marked with white arrows in Fig. 1(a-2)). Further prolonging the time to 1×10^4 h, both the particle size and volume fraction of α′ particles increase, being $r = 1.0$ nm and $f = 5.1\%$ (Fig. 1(a-3)). When the Cr content is higher than 20 at%, it is easy to precipitate the α′ nanoparticles, as seen in 22Cr, 28Cr, and 40Cr alloys (Fig. 1(b∼c)). For example, the volume fraction and particle size in the 28Cr alloy have already reached $f = 8.7\%$ and $r = 0.6$ nm in a 0.3×10^4 h-aged state, respectively. By comparing these alloys in a 1×10^4 h-aged state, it can be found that the volume fraction of the α′ phase increases with the Cr content, as evidenced by $f = 8.2\%$ in 22Cr and $f = 12.6\%$ in the 40Cr alloy. While the particle sizes of spherical α' precipitates in these alloys are comparable, being.

$r = 0.9 \sim 1.0$ nm. It is noted that in the 40Cr alloy, the α′ precipitates exhibit a worm-like morphology, rather than the spherical shape, which is ascribed to the difference of phase transition mechanisms induced by the larger difference in the free energies (G) between α and α′ phases of different Cr content alloys. In fact, low Cr (< 15Cr) alloys usually exhibit a nucleation growth mode ($\frac{\partial^2 G}{\partial c_{Cr}^2} > 0$), while high Cr alloys (> 20Cr) exhibit spinodal decomposition mode ($\frac{\partial^2 G}{\partial c_{Cr}^2} < 0$). Fig. 3(a) exhibits the

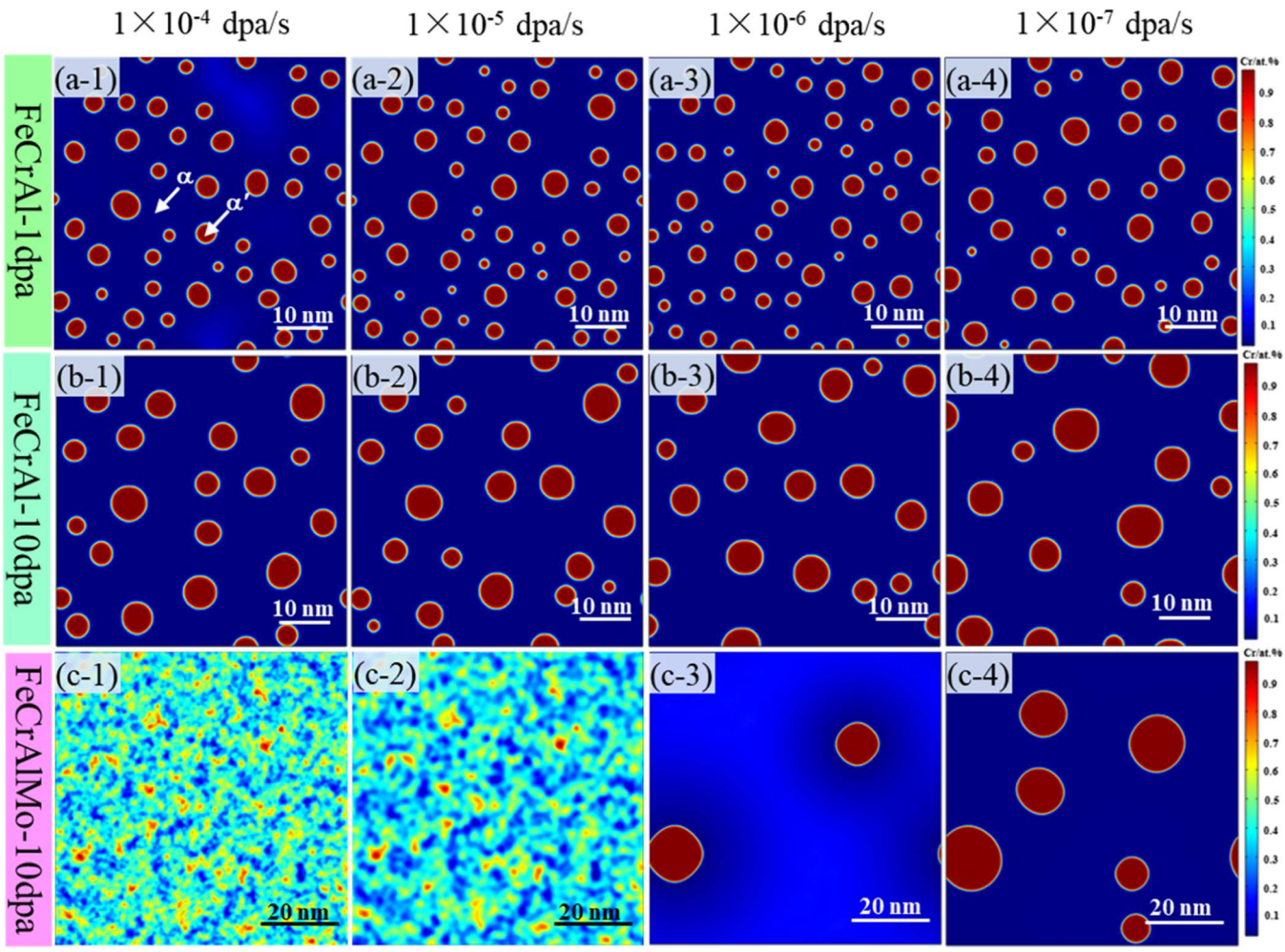

Fig. 6. Evolution of α′ nanoprecipitates in Fe-15.625Cr-9.375Al and Fe-13.889Cr-9.375Al-1.736Mo alloys irradiated to 10 dpa at different dose rates. (1): 1×10^{-4} dpa/s, (2): 1×10^{-5} dpa/s, (3): 1×10^{-6} dpa/s, and (4): 1×10^{-7} dpa/s.

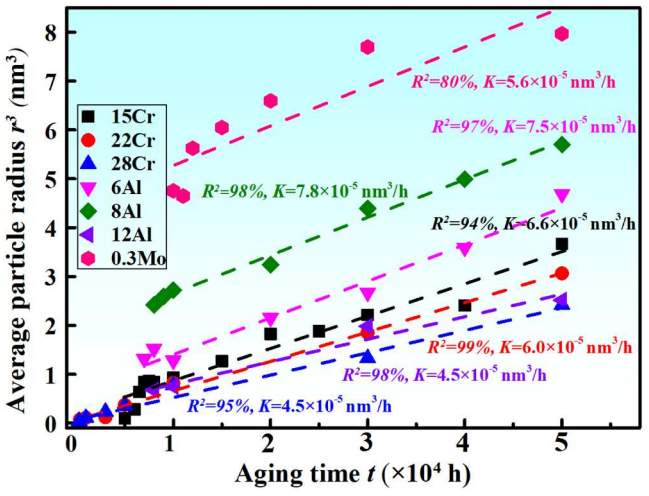

Fig. 7. Variation of the average particle radius (r^3) with the aging time in designed alloys, in which the fitted coarsening rate constant K and coefficient of determination R^2 are also marked.

variations of both the particle size and volume fraction of α′ precipitates with the aging time up to 5×10^4 h. And the time for the alloy to start precipitating the α′ phase is counted to evaluate the rate of phase separation at different Cr contents, and this time is named as the incubation time t_I. It is found that the incubation time (t_I) of α′-phase precipitates decrease from 5000 h in the 15Cr alloy, to 300 h in the 22Cr alloy, then to 200 h in the 28Cr alloy, which indicates that the increase of the Cr content can accelerate the precipitation of the α′ phase. After 1×10^4 h-aging, the volume fraction of α′ precipitates in each alloy did not vary with the aging time, implying that the microstructures in this series of alloys are stable. In addition, the number density of precipitates increases slightly from the 4.3×10^{24} m^{-3} in the 15Cr alloy to 5.7×10^{24} m^{-3} in the 22Cr alloy and 1.2×10^{25} m^{-3} in the 28Cr alloy, as seen in Fig. S1 (the Supplementary Materials). All these results indicate that the increase of the Cr content can promote the precipitation of the α′ phase.

4.1.2. α′ precipitation in Al-series of alloys

In order to explore the effect of the variation of Al content in Fe-Cr-Al alloys on the α′ phase precipitation, the Al-series of alloys with the compositions of Fe-15.625Cr-xAl (x = 6.25, 8.125, and 12.5 at%) were selected, being designated as 6Al, 8Al, and 12Al, respectively, in which the Cr content was fixed at a moderate value. Fig. 4 gives the morphology evolution of Cr-rich α′ precipitates with the aging time (0.6 ~ 5×10^4 h) at 573 K, from which it can be seen that the spherical α′ nanoparticles in this series of alloys do not precipitate from the BCC-α matrix until 0.6×10^4 h-aging. Fig. 3(b) describe the variations of the particle size and volume fraction of α′ nanoparticles with the aging time, showing an increasing tendency to 1×10^4 h and then being constant even when the time prolongs to 5×10^4 h in each alloy. Furthermore, the

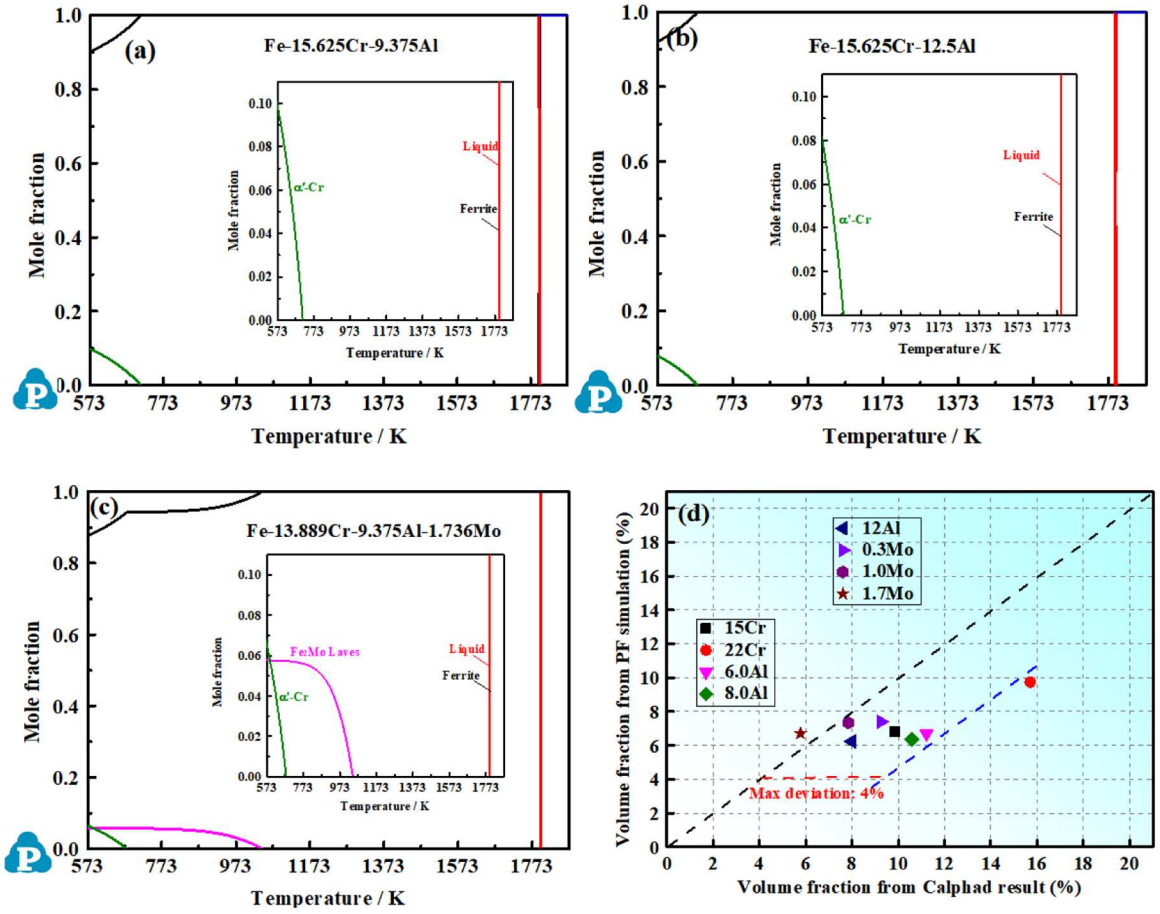

Fig. 8. Equilibrium-phase diagrams of $Fe_{75}Cr_{15.625}Al_{9.375}$ (a), $Fe_{71.875}Cr_{15.625}Al_{12.5}$ (b), and $Fe_{75}Cr_{13.889}Al_{9.375}Mo_{1.736}$ (at%) (c) alloys calculated by the Pandat software [54], in which the volume fraction values of α′ nanoprecipitates in the designed alloys obtained from phase diagrams were compared with those calculated from phase-field simulations, as presented in (d).

volume fraction values of α′ precipitates do not vary with the Al content, remaining a lower value of $f = 6 \sim 7\%$. However, the particle size reduces slightly with the Al, as presented by $r = 1.8$ nm for 6Al, $r = 1.7$ nm for 8Al, and $r = 1.4$ nm for 12Al in a 5×10^4 h-aged state, respectively. Combined with the basic Fe-15.625Cr-9.375Al alloy, the addition of Al can effectively inhibit the coarsening of α′ nanoparticles, i.e., reducing the risk of the α-α′ phase separation.

4.1.3. α′ precipitation in Mo-series of alloys.

Fig. 5 shows the morphology evolution of α′ precipitates in the Mo-containing alloys with the compositions of Fe-(15.625-x)Cr-9.375Al-xMo (x = 0.31, 1.042, and 1.736 at%) during aging at 573 K, in which the microstructural variation of the basic Fe-15.625Cr-9.375Al alloy without Mo was also given for comparison. It is found that the variation of α′ precipitates with aging time in the 0.3Mo alloy is similar to that in the basic alloy, and the particle size and volume fraction are also comparable with $f = 6.9\%$ and $r = 2.2$ nm in the 1×10^5 h-aged state for the 0.3Mo alloy and $f = 6.8\%$ and $r = 1.9$ nm for the basic alloy, which shows that low Mo content have less effect on phase separation. However, with increasing the Mo content, the incubation time for α′ precipitation will be prolonged, as evidenced by the fact that the incubation time increases from 0.5×10^4 h in the 0.3Mo alloy, to 2×10^4 h in the 1.0Mo alloy, then to 5×10^4 h in the 1.7Mo alloy. It indicates that the addition of Mo to substitute for Cr can obviously delay the precipitation of the α′ phase. Although the volume fraction values of α′ precipitates in this Mo-series of alloys are comparable ($f = 6 \sim 7\%$) after a long-time (1×10^5 h) aging, the particle size increases significantly with the Mo content, being from $r = 2.2$ nm in 0.3Mo to $r = 3.2$ nm in 1.0Mo, and then to $r = 4.3$ nm in the 1.7Mo alloy (Fig. 3(c)). More clearly, the number density of particles decreases from 1.4×10^{24} m^{-3} in the 0.3Mo alloy to 1.8×10^{23} m^{-3} in the 1.7Mo alloy (Fig. S1), which means that the latter is one tenth of the former. Although the particle size increased significantly with the increase of Mo content, the incubation time of α′ precipitation was prolonged, which significantly inhibited phase separation. Therefore, it can be deduced that the Mo content should be tailored to an appropriate value ($1 \sim 2$ at%) for inhibiting both the precipitation of the α′ phase and the coarsening of α′ particles.

In addition, the elemental distribution in the 1.0Mo alloy was also analyzed, as presented in Fig. 2(b), from which it can be seen that the Cr element is primarily segregated in the α′ phase with the content exceeding 90 at%, being consistent with that in the basic alloy (Fig. 2(a)). Interestingly, the Mo element is mainly enriched at the interface between α and α′ phases, neither in α nor α′. Such a phenomenon has been verified in the existing experimental results, as exemplified that the Mo element was enriched at the interface between the residual FCC austenitic phase and the BCC martensitic matrix in the Fe-11Cr-8Ni-5Co-2.5Mo alloy (wt%). Intrinsically, it was controlled by the diffusion of alloying elements [52].

4.2. Precipitation of the α′ phase in designed alloys at 573 K with irradiation

In order to investigate the α-α′ phase separation under an irradiation environment, we simulated the morphology evolution of α′ precipitates in irradiated Fe-Cr-Al-based alloys (the basic alloy and 1.7Mo alloy) with different irradiation doses ($1 \sim 10$ dpa) and dose rates (1×10^{-7} to 1×10^{-4} dpa/s), as presented in Figs. 6 and 3(d). For the basic Fe-

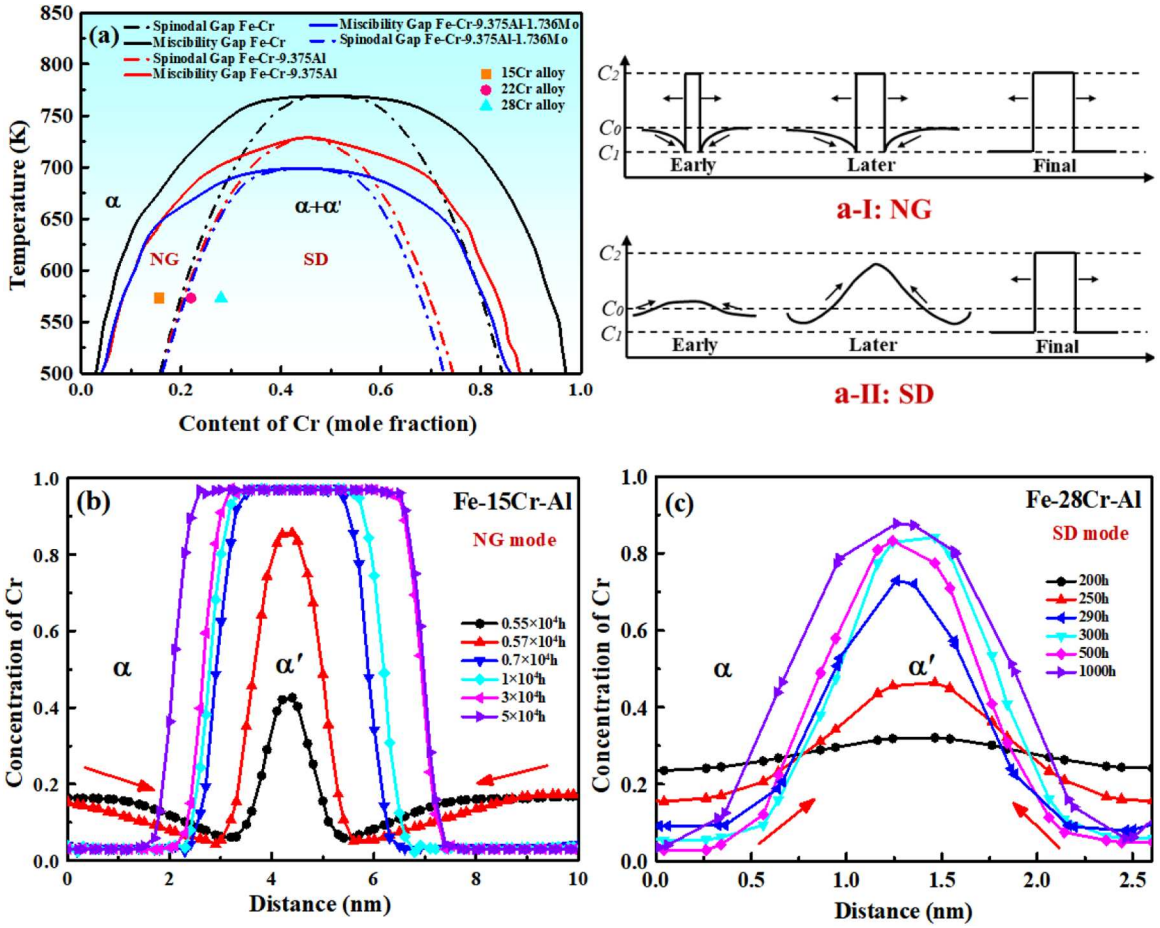

Fig. 9. (a): Miscibility gaps (solid lines) in different Fe-Cr-Al-Mo alloys, in which the dotted line in each miscibility gap divides the α-α′ phase separation into the nucleation-growth (NG) mode and spinodal-decomposition (SD) mode, and the schematic diagrams of the concentration change for NG and SD modes are given in (a-I) and (a-II) [56]; (b, c): Variations of the Cr content in the α′ phase with the aging time in the NG mode for the Fe-15.625Cr-9.375Al alloy and SD mode for the Fe-28.125Cr-9.375Al alloy.

15.625Cr-9.375Al alloy, the irradiation accelerates the precipitation and coarsening of α′ particles, as evidenced by the fact that the incubation time for the α′ precipitation was reduced drastically from 5000 h in the aged state to 2 ~ 388 h in the irradiated state with different dose rates of $1\times10^{-7} \sim 1\times10^{-4}$ dpa/s. Moreover, the average particle size increases from $r = 1.5$ nm in a 1 dpa-irradiated state with the dose rate of 1×10^{-4} dpa/s (2.77 h in Fig. 6(a-1)) to $r = 2.4$ nm in a 10 dpa-irradiated state (27.7 h in Fig. 6(b-1)), while the particle size in the aged state is only $r = 1.0$ nm even after 1×10^{4} h-aging. Besides the irradiation dose, the irradiation dose rate has also a significant influence on the α′ precipitation. The incubation time for the α′ precipitation could be reduced with the increase of the dose rate, being from 388.8 h (0.14 dpa) at the rate of 1×10^{-7} dpa/s, to 69.4 h (0.25 dpa) at 1×10^{-6} dpa/s and to 8.3 h (0.3 dpa) at 1×10^{-5} dpa/s, then to 1.4 h (0.5 dpa) at 1×10^{-4} dpa/s, progressively. A similar trend also occurs in the particle size, from $r = 2.9$ nm at 1×10^{-7} dpa/s to $r = 2.4$ nm at 1×10^{-4} dpa/s. However, the volume fraction of α′ precipitates does not vary with the irradiation dose rate, still remaining a lower value of $f \sim 7\%$. For the 1.7Mo alloy, there does not appear the α-α′ phase separation after being irradiated to 1 dpa at the different dose rates of $1\times10^{-7} \sim 1\times10^{-4}$ dpa/s. Even after being irradiated up to 10 dpa, the α-α′ phase separation is not obvious yet at high dose rate ($1\times10^{-5} \sim 1\times10^{-4}$ dpa/s), which could occur at a relatively-low dose rate ($< 10^{-6}$ dpa/s) alone (Fig. 6(c)). Among them, the average particle size and volume fraction of α′ precipitates are $r = 5.7$ nm and $f = 7.3\%$ at the dose rate of 1×10^{-7} dpa/s. All these results indicate the irradiation dose can accelerate the precipitation of the α′ phase in low-Cr alloys, while the irradiation dose rate plays an opposite role for the α-α′ phase separation, which is difficult to occur at a high dose rate of $1\times10^{-5} \sim 1\times10^{-4}$ dpa/s for the Fe-Cr-Al-Mo alloy.

5. Discussion

5.1. Coarsening kinetics of α′ precipitates in designed alloys

From above observations, it is known that the volume fraction of α′ particles in the current alloy series remains almost constant with the aging-time prolonging. Thus, the classic Ostwald ripening theory proposed by Philippe and Voorhees (PV theory) could be applied to study the coarsening behavior of α′ particles [53]. Such a time-dependent coarsening process could be described with the following Eq. (12):

$$r(t)^3 - r(t_0)^3 = K(t - t_0) \tag{12}$$

where $r(t)$ is the average particle radius at time t, K is the coarsening rate constant, t_0 represents the beginning time of coarsening. Fig. 7 gives the variation of the size (r^3) of α′ particles with the time (t) in different series of alloys, which could be well fitted by the PV theory. It is found that the values of the coarsening-rate constant in these current alloys are all comparable, within a range of $K = (4.5 \sim 8.0)\times10^{-5}$ nm^3/h. In addition, since the α′ particles are mainly enriched by the Cr element, and the coarsening process of α′ nanoparticles might be related to the atomic mobility of Cr in the BCC matrix. In fact, the atomic mobility of Cr calculated by Eq. (5) in each alloy series are also within a narrow range of $(5.3 \sim 13.0)\times10^{-28}$ m^2/s. Therefore, the coarsening behavior of α′

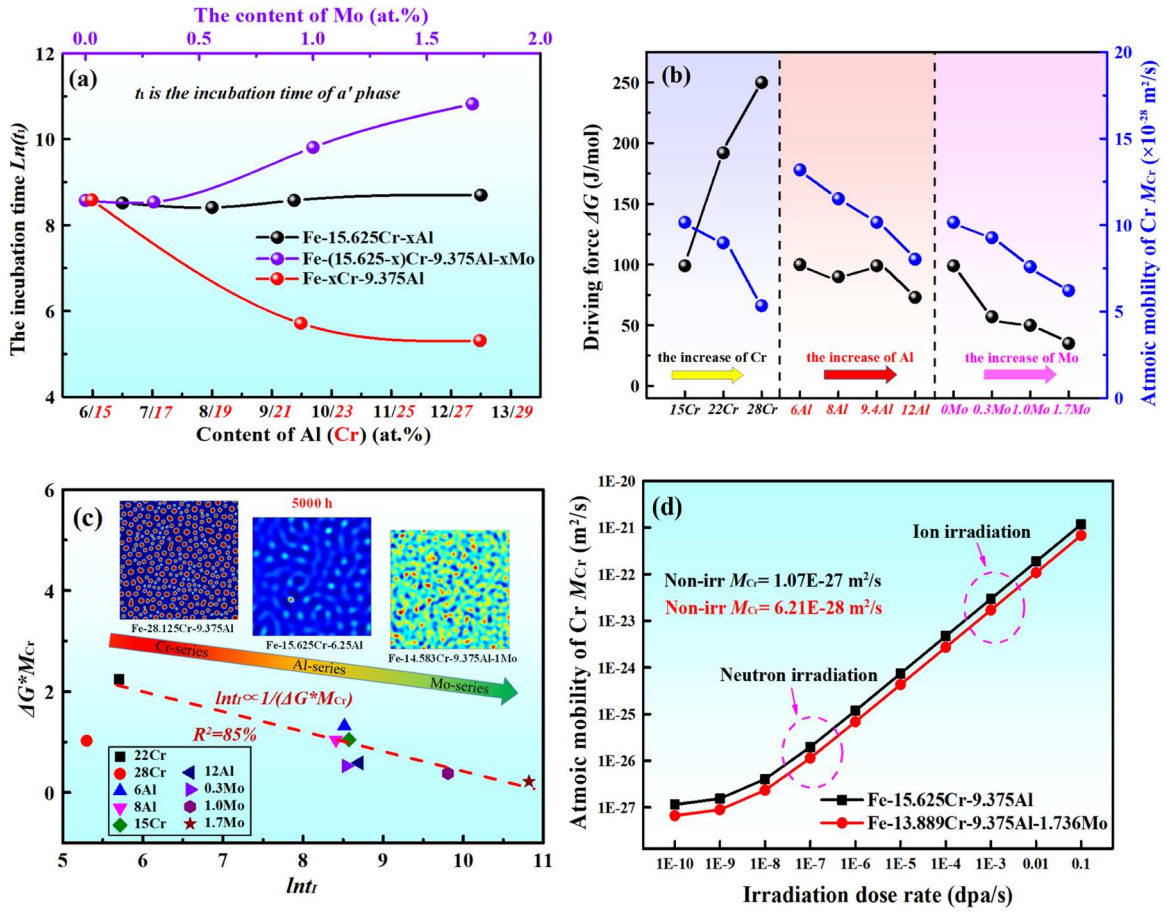

Fig. 10. (a): Variation of the incubation time (lnt_I) for α′ precipitation with the content of Al or Cr in designed alloy series; (b): Variations of the driving force (ΔG) for the α-α′ phase separation and the atomic mobility of Cr (M_{Cr}) with the content of alloying element in designed alloy series; (c): Relationship between lnt_I and ΔG^*M_{Cr} for the α′ precipitation; and (d): Variation of M_{Cr} in the designed alloys with the irradiation dose rate.

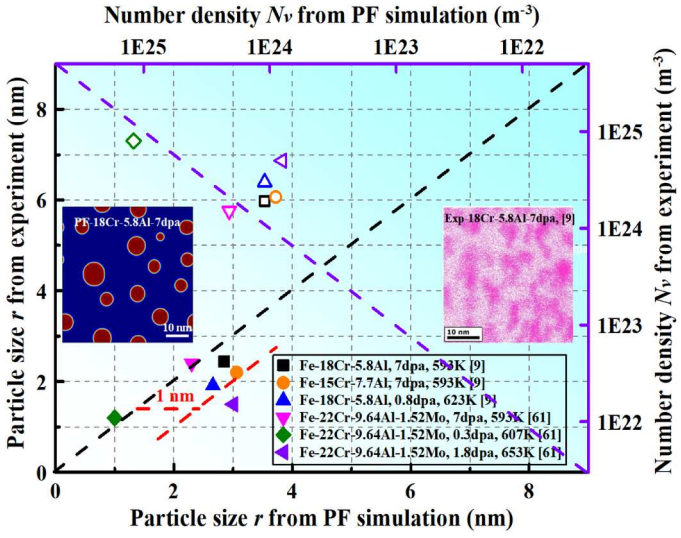

Fig. 11. Comparison of the average particle radius r and number density Nv of α′ nanoprecipitates in Fe-Cr-Al-Mo alloys obtained from the experimental results with those from the PF simulations, in which the experimental results were taken from Refs. [9,61]. And the hollow data points represent the number density, solid data points represent the particle size.

nanoparticles in these alloy series is similar, showing a comparable coarsening rate during the thermal-aging process.

5.2. *Effect of alloying elements on α′-phase precipitation in designed alloys*

The thermodynamic-phase diagram calculations were conducted to study the effect of alloying elements on the phase constitution in the designed alloys, as presented in Fig. 8, giving the equilibrium phase diagrams of typical $Fe_{75}Cr_{15.625}Al_{9.375}$, $Fe_{71.875}Cr_{15.625}Al_{12.5}$, and $Fe_{75}Cr_{13.889}Al_{9.375}Mo_{1.736}$ (at%) alloys calculated by the Pandat thermodynamic software [54]. It can be seen that the α′-Cr phase exists in all these alloys when the temperature is below 723 K. Moreover, the molar fraction of the α′ phase drops from 9.8% in the 9.375Al alloy to 8.0% in the 12.5Al alloy with increasing the Al content. When the Mo element was added to replace the Cr, the molar fraction of α′ drops down to 5.8% in the 1.7Mo alloy obviously. Also, the hexagonal Fe_2Mo Laves phase ($MgZn_2$-type) exists within a wide temperature range of 573 ~ 1073 K (Fig. 8(c)), which has been proved by existing studies that the addition of Mo could form the Fe_2Mo Laves phase [1,3]. The current PF simulation results (Figs. 4 and 5) indicate that both Al and Mo elements could inhibit and delay the precipitation of the α′ phase, which is consistent with the thermodynamic calculations. Fig. 8(d) gives a comparison of the volume fraction of the α′ phase calculated by the PF method and the thermodynamic calculations, and the maximum deviation is about ~ 4%, which could be acceptable when considering the statistical and computational errors.

In order to further analyze the influence of different elements on the α-α′ phase separation in Fe-Cr-Al-based alloys, the miscibility gaps in

different alloys were drawn in Fig. 9(a), where the solid line is obtained by calculating the common tangent region on the energy curve and the dashed line is derived by calculating the region of $\frac{\partial^2 G}{\partial c_{Cr}^2} < 0$ [55]. The α-α′ phase separation occurs in the range of 3 ~ 96 at% Cr for the Fe-Cr binary system below 770 K (a black solid line), while the addition of Al in Fe-Cr binary alloys can reduce both the critical temperature (728 K) and the composition region (4 ~ 88 at% Cr, red line) of phase separation. And the addition of Mo further decreases the critical temperature down to 700 K, and the miscibility gap is in the range of 4 ~ 86 at% Cr (blue line). The shrinkage of the miscibility gap implies that the α-α′ phase separation is more difficult to occur with the additions of Al and Mo elements. In fact, there are two mechanisms of nucleation-growth (NG) and spinodal decomposition (SD) in the miscibility gap (Fig. 9(a-I, a-II)), in which the range marked within dotted line is controlled by the SD mechanism and the range between the solid and dotted lines is controlled by the NG mechanism [56]. For the Cr-series of Fe-xCr-9.375Al alloys, with increasing the Cr content, the phase precipitation could change from the NG to SD mode, as evidenced by the positions of alloy compositions in Fig. 9(a). It can be seen that the change of the Cr concentration of the α′ phase near the interface region in the 15Cr alloy shows a downhill diffusion, as marked with red arrows in Fig. 9(b). The interface between the α and α′ phases is obvious at the initial stage during aging and the width of particles increases gradually with the aging time, which is consistent with the concentration variation of the typical NG mode. By contrast, the Cr concentration near the α-α′ interface in the 28Cr alloy shows an uphill diffusion (Fig. 9(c)) since there is no obvious interface between α/α′ and the composition fluctuation is continuous, belonging to the typical SD mode.

Besides, the modulation of alloying elements M (M = Cr, Al, and Mo) also affects significantly the incubation time of the α-α′ phase separation. Fig. 10(a) shows the variation of the incubation time (t_I) for α′ precipitation with the M content. Obviously, the incubation time, $ln\ (t_I)$, decreases with the increase of Cr content, while it increases with the Mo content. And the change of Al has little effect on the incubation time since the $ln(t_I)$ values keep almost constant. Moreover, the effect of M elements on the α-α′ phase separation was also illustrated from the viewpoints of both thermodynamics (Gibbs free energy) and kinetics (atomic mobility). Fig. 10(b) gives the values of the driving forces for the phase transformation from the α to α+α′ ($\Delta G = |G_\alpha\text{-}G_{\alpha+\alpha'}|$) and the atomic mobility of Cr element (M_{Cr}) in the Cr-series, Al-series, and Mo-series of alloys, where the ΔG was obtained from the Gibbs free-energy curve drawn with Eq. (3) (Fig. S2), and the M_{Cr} was calculated with Eq. (5). It can be seen that the driving force, increases from $\Delta G = 103$ J/mol in the 15Cr alloy to $\Delta G = 250$ J/mol in the 28Cr alloy, and drops drastically down to $\Delta G = 35$ J/mol in the 1.7Mo alloy. However, the ΔG values don't vary with the Al content, being $\Delta G \sim 100$ J/mol. For the atomic mobility of the Cr element, it slightly decreases with the M content in each alloy series with the value in the range of $(5.3 \sim 13.0)\times 10^{-28}$ m^2/s. So, it could be predictable that the $ln\ (t_I)$, ΔG, and M_{Cr} follows the relationship of $lnt_I \propto 1/(\Delta G^* M_{Cr})$, as presented in Fig. 10(c), which was obtained by fitting the current data. This declining trend is in a good consistence with the simulated results (the inset of Fig. 10(c)). It is noted that there exists a slight difference in the 28Cr alloy, which might be ascribed to that the mechanism of the α-α′ phase separation is dominated by the spinodal decomposition, rather than the nucleation and growth mode. Therefore, the increase in the incubation time, t_I, for the α′ precipitation is related to the decrease of ΔG and M_{Cr}, which could be realized by tailoring the content of alloying elements.

5.3. Effect of irradiation on α-α′ phase separation

By comparing the simulated results under thermal-aging conditions with those under irradiation, the α-α′ phase separation is indeed accelerated by irradiation. Experimentally, both neutron and heavy-ion irradiations can produce a large amount of vacancies and interstitials, which seriously accelerates the diffusion of alloying elements [15]. Thus, the RED model was introduced to establish the relationship between the diffusion coefficient and irradiation-dose rate to uncover the effect of the irradiation dose on the phase separation. Fig. 10(d) gives the atomic mobility of the Cr element M_{Cr} under different dose rates, from which it can be seen that the M_{Cr} in the Fe-15.625Cr-9.375Al alloy increases from the 1.07×10^{-27} m^2/s in a non-irradiated state to 1.97×10^{-26} m^2/s at the dose rate of 1×10^{-7} dpa/s, and then to 2.95×10^{-23} m^2/s at 1×10^{-3} dpa/s, which ultimately leads to a significant acceleration of the α-α′ phase separation with the incubation time reduced from 5000 h in the aged state to 2 ~ 388 h in the irradiated states. And the same trend was also observed in the Fe-Cr-Al-Mo alloy (Fig. 10(d)). Compared with heavy-ion irradiation with a high dose rate (~ 1×10^{-3} dpa/s), the neutron irradiation with a lower dose rate (~ 1×10^{-7} dpa/s) will more easily to induce the phase separation at the same irradiation dose due to that the low dose rate leads to a longer irradiation time. In fact, this trend has been demonstrated by existing experimental results that the α′ phase appeared in Fe-15Cr alloy after being neutron-irradiated to 1.82 dpa with a dose rate of 3.4×10^{-7} dpa/s and at 573 K, while it did not appear when being irradiated by Fe ions even up to 60 dpa with a dose rate of 1×10^{-4} dpa/s [10,57–60].

In order to verify the accuracy of the current phase-field model, the α′-phase precipitation in existing Fe-18Cr-5.8Al, Fe-15Cr-7.7Al and Fe-22Cr-9.64Al-1.52Mo (at%) alloys after being irradiated at different temperatures (593 ~ 653 K) with different doses (0 ~ 7 dpa) and the dose rate of ~ 7.9×10^{-7} dpa/s were simulated, as presented in Figs. S3 and S4, in which the related experimental results were also reproduced [9,61]. The simulated results were then compared with the experiments, including the number density (Nv) and particle size (r) of α′ nanoprecipitates, as shown in Fig. 11. It can be seen that the Nv value of α′ nanoprecipitates in each alloy obtained by the simulation keeps in an order of magnitude with the experimental result (1×10^{24} ~ 1×10^{25} m^{-3}), and the particle sizes in both cases are also well consistent with the deviation less than 1 nm. Therefore, the current RED-embedded phase-field model can well simulate and predict nuclear Fe-Cr-Al-based alloys under both thermal-aging and irradiation conditions.

6. Conclusions

The present work applied the phase-field method based on the Cahn-Hilliard equation and radiation-enhanced diffusion model to simulate the α-α′ phase separation in nuclear Fe-Cr-Al-based alloys. Three series of alloys, Fe-xCr-9.375Al (Cr-series), Fe-15.625Cr-xAl (Al-series), and Fe-(15.625-x)Cr-9.375Al-xMo (Mo-series), were designed to reveal the effect of alloying elements (Cr, Al, and Mo) on the α′ precipitation under both thermal-aging and irradiation conditions. The following conclusions could be drawn.

1) The α-α′ phase separation is closely related to the species and amounts of alloying elements during thermal aging. The increase of Cr content in Cr-series of alloys accelerates the α-α′ phase separation, as evidenced by the increase in the volume fraction of α′ nanoprecipitates (from 5.1% in 15Cr to 12.6% in 40Cr) and the reduction in the incubation time for α′ precipitation (from 5000 h in 15Cr to 200 h in 28Cr) when aging at 573 K. The change of Al content in Al series of alloys can effectively inhibit the coarsening of α′ nanoparticles with the volume fraction (6 ~ 7%) and incubation time (5000 ~ 6000 h) keeps almost constant. While the substitution of Mo for Cr can obviously delay the phase separation in Mo series of alloys since the incubation time extends from 0.5×10^4 h in 0.3Mo to 5×10^4 h in the 1.7Mo alloy. In addition, the particle sizes of α′ precipitates in all these series of alloys show a gradually increasing trend with the value in the range of $r = 1 \sim 3$ nm.
2) The irradiation accelerates the α-α′ phase separation significantly, which is closely related to both the irradiation dose and dose rate.

The incubation time for α′ precipitation reduces to 2 ~ 388 h (0.14 ~ 0.5 dpa) in 15Cr alloy at the dose rate of 1×10^{-7} ~ 1×10^{-4} dpa/s, and the particle size is coarsened up to 2.4 ~ 2.9 nm after being irradiated to 10 dpa, which is ascribed to the increase in the atomic mobility of the Cr element caused by the radiation-enhanced diffusion. By contrast, the Fe-13.899Cr-9.375Al-1.736Mo alloy possesses the best irradiation resistance due to that the α′ precipitation is not obvious yet even after being irradiated up to 10 dpa at a high dose rate ($> 1\times10^{-5}$ dpa/s), which occurs at a relatively-low dose rate ($< 10^{-6}$ dpa/s) alone.

3) The analysis on the influencing factors of the α-α′ phase separation demonstrates that the incubation time (t_I) for the α′ precipitation is strongly dependent on the driving force (ΔG) of α→(α+α′) transformation and the atomic mobility (M_{Cr}) of Cr element. The relationship between them follows a negative correlation of $ln(t_I) \propto 1/(\Delta G^* M_{Cr})$.
4) The present phase-field model is also used to simulate the α-α′ phase separation in existing typical Fe-Cr-Al-based alloys in different irradiated states, and the simulations are well consistent with experimental results. Therefore, the present phase-field model can play a significant role in predicting the phase separation in novel nuclear Fe-Cr-Al-based alloys.

CRediT authorship contribution statement

Ben Niu: Writing – original draft, Methodology, Investigation, Formal analysis, **Zhen Li**: Methodology, Data curation, **Qing Wang**: Writing – review & editing, Supervision, Conceptualization, **Zhenhua Wang**: Data curation, **Sen Ge**: Methodology, **Chuang Dong**: Resources, Formal analysis, **Ruiqian Zhang**: Conceptualization, **Donghui Wen**: Formal analysis, **Huiqun Liu**: Formal analysis, **Peter K. Liaw**: Visualization.

Declaration of Competing Interest

The authors declare that they have no known competing financial interests or personal relationships that could have appeared to influence the work reported in this paper.

Data availability

Data will be made available on request.

Acknowledgments

It was supported by the National Natural Science Foundation of China (U1867201, 52171152 and 52201175). PKL very much appreciates the support from the National Science Foundation (DMR – 1611180, 1809640, and 2226508).

Appendix A. Supporting information

Supplementary data associated with this article can be found in the online version at doi:10.1016/j.mtcomm.2024.108431.

References

[1] Y. Yamamoto, B.A. Pint, K.A. Terrani, K.G. Field, Y. Yang, L.L. Snead, Development and property evaluation of nuclear grade wrought FeCrAl fuel cladding for light water reactors, J. Nucl. Mater. 467 (2015) 703–716.
[2] S.J. Zinkle, G.S. Was, Materials challenges in nuclear energy, Acta Mater. 61 (2013) 735–758.
[3] Z.Q. Sun, P.D. Edmondson, Y. Yamamoto, Effects of Laves phase particles on recovery and recrystallization behaviors of Nb-containing FeCrAl alloys, Acta Mater. 144 (2018) 716–727.
[4] S. Kobayashi, T. Takasugi, Mapping of 475°C embrittlement in ferritic Fe-Cr-Al alloys, Scr. Mater. 63 (2010) 1104–1107.
[5] J.K. Sahu, U. Krupp, R.N. Ghosh, H.J. Christet, Effect of 475°C embrittlement on the mechanical properties of duplex stainless steel, Mater. Sci. Eng. A 508 (2009) 1–14.
[6] C. Capdevila, M.K. Miller, I. Toda, J. Chao, Influence of the α-α′ phase separation on the tensile properties of Fe-base ODS PM 2000 alloy, Mater. Sci. Eng. A 527 (2010) 7931–7938.
[7] G. Bonny, D. Terentyev, L. Malerba, On the α-α′ miscibility gap of Fe-Cr alloys, Scr. Mater. 59 (2008) 1193–1196.
[8] Z. Yang, Z.X. Wang, C.H. Xia, M.H. Ouyang, J.C. Peng, H.W. Zhang, X.S. Xiao, Aluminum suppression of α′ precipitate in model Fe-Cr-Al alloys during long-term aging at 475 °C, Mater. Sci. Eng. A 772 (2020) 138714.
[9] S.A. Briggs, P.D. Edmondson, K.C. Littrell, Y. Yamamoto, R.H. Howard, C.R. Daily, K.A. Terrani, K. Sridharan, K.G. Field, A combined APT and SANS investigation of α′ phase precipitation in neutron-irradiated model FeCrAl alloys, Acta Mater. 129 (2017) 217–228.
[10] M. Bachhav, G.R. Odette, E.A. Marquis, α′ precipitation in neutron-irradiated Fe-Cr alloys, Scr. Mater. 74 (2014) 48–51.
[11] J. Ejenstam, M. Thuvander, P. Olsson, F. Rave, P. Szakalos, Microstructural stability of Fe-Cr-Al alloys at 450-550°C, J. Nucl. Mater. 457 (2015) 291–297.
[12] P. Dou, Z.X. Xin, W. Sang, A. Kimurat, Age-hardening mechanisms of 15Cr ODS ferritic steels with 5, 7 and 9 wt% Al at 475 °C for 9000h, J. Nucl. Mater. 540 (2020) 152368.
[13] Z.Q. Sun, H.B. Bei, Y. Yamamoto, Microstructural control of FeCrAl alloys using Mo and Nb additions, Mater. Charact. 132 (2017) 126–131.
[14] W.Y. Chen, Y.B. Miao, Y.Q. Wu, C.A. Tomchik, K. Mo, J. Gan, M.A. Okuniewski, S. A. Maloy, J.F. Stubbins, Atom probe study of irradiation-enhanced α′ precipitation in neutron-irradiated Fe-Cr model alloys, J. Nucl. Mater. 462 (2015) 242–249.
[15] F. Soisson, T. Jourdan, Radiation-accelerated precipitation in Fe-Cr alloys, Acta Mater. 103 (2016) 870–881.
[16] J.E. Westraadt, E.J. Olivier, J.H. Neethling, P. Hedström, J. Odqvist, X. Xu, A. Steuwer, A high-resolution analytical scanning transmission electron microscopy study of the early stages of spinodal decomposition in binary Fe-Cr, Mater. Charact. 109 (2015) 216–221.
[17] J.L. Li, Z. Li, Q. Wang, C. Dong, P.K. Liaw, Phase-field simulation of coherent BCC/B2 microstructures in high entropy alloys, Acta Mater. 197 (2020) 10–19.
[18] S.J. Shi, Z.W. Yan, Y.S. Li, S. Muhammad, D. Wang, S. Chen, S.S. Jin, Phase-field simulation of early-stage kinetics evolution of γ′ phase in medium supersaturation Co-Al-W alloy, J. Mater. Sci. Technol. 53 (2020) 1–12.
[19] G.M. Han, Z.Q. Han, A.A. Luo, A.K. Sachdev, B. Liu, A phase field model for simulating the precipitation of multi-variant β-$Mg_{17}Al_{12}$ in Mg-Al-based alloys, Scr. Mater. 68 (2013) 691–694.
[20] M. Mccormack, A.G. Khachaturyan, J.W. Morris, A two-dimensional analysis of the evolution of coherent precipitates in elastic media, Acta Metall. Mater. 40 (1992) 325–336.
[21] J. Kundin, L. Mushongera, T. Goehler, H. Emmerich, Phase-field modeling of the γ′-coarsening behavior in Ni-based superalloys, Acta Mater. 60 (2012) 3758–3772.
[22] Z.L. Yan, Y.S. Li, X.R. Zhou, Y.D. Zhang, R. Hu, Evolution of nanoscale Cr-rich phase in a Fe-35 at% Cr alloy during isothermal aging, J. Alloy. Compd. 725 (2017) 1035–1043.
[23] Y.S. Li, Z.L. Yan, X.R. Zhou, Kinetics of initial phase separation and coarsening of nanoscale phase in Fe-Cr alloys, J. Nucl. Mater. 497 (2017) 154–160.
[24] S. Chen, Y.S. Li, S.J. Shi, S.S. J, Quantitative phase-field simulation of composition partition and separation kinetics of nanoscale phase in Fe-Cr-Al alloy, J. Nanomater. 2019 (2019) 6862390.
[25] Y. Ma, Q. Wang, C.L. Li, L.J. Santodonato, M. Feygenson, C. Dong, P.K. Liaw, Chemical short-range orders and the induced structural transition in high-entropy alloys, Scr. Mater. 144 (2018) 64–68.
[26] C. Pang, B.B. Jiang, Y. Shi, Q. Wang, C. Dong, Cluster-plus-glue-atom model and universal composition formulas [cluster](glue atom)x for BCC solid solution alloys, J. Alloy. Compd. 652 (2015) 63–69.
[27] Z. Li, D.H. Wen, Y. Ma, Q. Wang, G.Q. Chen, R.Q. Zhang, R. Tang, H. He, Prediction of alloy composition and microhardness by random forest in maraging stainless steels based on a cluster formula, J. Iron Steel Res. Int. 25 (2018) 717–723.
[28] T. Yang, Y.L. Zhao, Y. Tong, Z.B. Jiao, J. Wei, J.X. Cai, X.D. Han, D. Chen, A. Hu, J. J. Kai, K. Lu, Y. Liu, C.T. Liu, Multicomponent intermetallic nanoparticles and superb mechanical behaviors of complex alloys, Science 362 (2018) 933–937.
[29] B. Niu, Z.H. Wang, Q. Wang, S. Ge, C. Dong, R.Q. Zhang, H.Q. Liu, P.K. Liaw, Effect of Zr addition on the stability of precipitated Laves phase and mechanical properties of Fe-Cr-Al-based alloys at high temperatures, Prog. Nat. Sci. Mater. 32 (2022) 114–127.
[30] J.W. Cahn, J.E. Hilliard, Free energy of a nonuniform system. I. Interfacial free energy, J. Chem. Phys. 28 (1958) 258–267.
[31] R.R. Mohanty, Y. Sohn, Phase-field investigation of multicomponent diffusion in single-phase and two-phase diffusion couples, J. Phase Equilib. Diffus. 27 (2006) 676–683.
[32] J.W. Cahn, Phase Separation by spinodal decomposition in isotropic systems, J. Chem. Phys. 42 (1965) 93–99.
[33] Z.L. Luo, Y. Du, Y.L. Liu, S. Tang, Y.F. Pan, H. Mao, Y.B. Peng, W.S. Liu, Z.K. Liu, Phase field simulation of the phase separation in the TiC-ZrC-WC system, Calphad 63 (2018) 190–195.
[34] A.T. Dinsdale, SGTE data for pure elements, Calphad 15 (1991) 317–425.
[35] M.H.G. Jacobs, R. Schmid-Fetzer, T. Markus, V. Motalov, G. Borchardt, K.-H. Spitzer, Thermodynamics and diffusion in ternary Fe-Al-Cr alloys, part I: thermodynamic modeling, Intermetallics 16 (2008) 995–1005.
[36] C.P. Guo, C.R. Li, P.J. Masset, Z.M. Du, A thermodynamic description of the Al-Mo-Si system, Calphad 36 (2012) 100–109.

[37] Z.M. Du, C.P. Guo, C.R. Li, W.J. Zhang, Thermodynamic description of the Al-Mo and Al-Fe-Mo systems, J. Phase Equilib. Diffus. 30 (2009) 487.
[38] T. Kitashima, H. Harada, A new phase-field method for simulating γ′ precipitation in multicomponent nickel-base superalloys, Acta Mater. 57 (2009) 2020–2028.
[39] K. Wu, J.E. Morral, Y. Wang, Movement of Kirkendall markers, second phase particles and the Type 0 boundary in two-phase diffusion couple simulations, Acta Mater. 52 (2004) 1917–1925.
[40] B. Jönsson, Assessment of the mobilities of Cr, Fe and Ni in bcc Cr-Fe-Ni Alloys, ISIJ Int. 35 (1995) 1415–1421.
[41] O. Redlich, A.T. Kister, Algebraic representation of thermodynamic properties and the classification of solutions, Ind. Eng. Chem. 40 (1948) 345–348.
[42] Y. Chen, L. Cheng, Y.L. Zhang, Assessment of atomic mobility for the Bcc phase of the Ti-Al-Mo system, IOP Conf. Series Mater. Sci. Eng. 242 (2017) 12019.
[43] W.B. Li, B. Tang, Y.W. Cui, R. Hu, H. Chang, J.S. Li, L. Zhou, Assessment of diffusion mobility for the bcc phase of the Ti-Al-Cr system, Calphad 35 (2011) 384–390.
[44] G. Lindwall, K. Frisk, Assessment and evaluation of mobilities for diffusion in the bcc Cr-Mo-Fe system, J. Phase Equilib. Diffus. 33 (2012) 375–389.
[45] Y. Chen, J.S. Li, B. Tang, H.C. Kou, J. Segurado, Y.W. Cui, Computational study of atomic mobility for bcc phase in Ti-Al-Fe system, Calphad 46 (2014) 205–212.
[46] E.A. Brandes, G.B. Brook. Smithells Metals Reference Book, 1983.
[47] G.R. Odette, T. Yamamoto, D. Klingensmith, On the effect of dose rate on irradiation hardening of RPV steels, Philos. Mag. 85 (2005) 779–797.
[48] J.H. Ke, E.R. Reese, E.A. Marquis, G.R. Odette, D. Morgan, Flux effects in precipitation under irradiation - simulation of Fe-Cr alloys, Acta Mater. 164 (2019) 586–601.
[49] H. Ke, P. Wells, P.D. Edmondson, N. Almirall, L. Barnard, G.R. Odette, D. Morgan, Thermodynamic and kinetic modeling of Mn-Ni-Si precipitates in low-Cu reactor pressure vessel steels, Acta Mater. 138 (2017) 10–26.
[50] L. Malerba, Molecular dynamics simulation of displacement cascades in α-Fe: a critical review, J. Nucl. Mater. 351 (2006) 28–38.
[51] COMSOL Multiphysics 5.4 User's Guide, COMSOL U.S.A., 2018.
[52] G. Liu, J. Su, A. Wang, Z.Y. Yang, Y.L. Ding, J. Ning, Q. Gao, A novel Fe-Cr-Ni-Co-Mo maraging stainless steel with enhanced strength and cryogenic toughness: role of austenite with core-shell structures, Mater. Sci. Eng. A 863 (2023) 144537.
[53] T. Philippe, P.W. Voorhees, Ostwald ripening in multicomponent alloys, Acta Mater. 61 (2013) 4237–4244.
[54] T.M. Pandat, Thermodynamic Calculations and Kinetic Simulations, CompuTherm LLC, WI, Madison, 2011.
[55] C. Capdevila, M.K. Miller, J. Chao, Phase separation kinetics in a Fe-Cr-Al alloy, Acta Mater. 60 (2012) 4673–4684.
[56] J.W. Cahn, Spinodal decomposition, Trans. AIME 242 (1968) 166.
[57] V. Kuksenko, C. Pareige, P. Pareige, Cr precipitation in neutron irradiated industrial purity Fe-Cr model alloys, J. Nucl. Mater. 432 (2013) 160–165.
[58] L.L. Horton, J. Bentley, W.A. Jesser, The microstructure of "triple-beam" ion irradiated Fe and Fe-Cr alloys, J. Nucl. Mater. 104 (1981) 1085–1089.
[59] C. Pareige, V. Kuksenko, P. Pareige, Behaviour of P, Si, Ni impurities and Cr in self ion irradiated Fe-Cr alloys - comparison to neutron irradiation, J. Nucl. Mater. 456 (2015) 471–476.
[60] E. Marquis, B. Wirth, G. Was, Characterization and Modeling of Grain Boundary Chemistry Evolution in Ferritic Steels under Irradiation, 2016.
[61] K.G. Field, K.C. Littrell, S.A. Briggs, Precipitation of α′ in neutron irradiated commercial FeCrAl alloys, Scr. Mater. 142 (2018) 41–45.